H₂S decomposition into H₂ and S₂ by plasma technology : comparison of gliding arc and microwave plasma

H₂S decomposition into H₂ and S₂ by plasma technology: Comparison of gliding arc and microwave plasma

Quan-Zhi Zhang[1,2], Weizong Wang[2,3], Christophe Thille[4], and Annemie Bogaerts[2]

[1]School of Physics, Dalian University of Technology, Dalian 116024, P.R. China
[2]Research group PLASMANT, Department of Chemistry, University of Antwerp, Universiteitsplein 1, B-2610 Wilrijk-Antwerp, Belgium
[3]School of Astronautics, Beihang University, 100191, Beijing, People's Republic of China
[4]Total Research and Technology Feluy, Zone Industrielle Feluy C, B-7181 Seneffe, Belgium
Email: qzzhang@dlut.edu.cn, wangweizong@gmail.com, annemie.bogaerts@uantwerpen.be

Abstract

We studied hydrogen sulfide (H_2S) decomposition into hydrogen (H_2) and sulfur (S_2) in a gliding arc plasmatron (GAP) and microwave (MW) plasma by a combination of 0D and 2D models. The conversion, energy efficiency, and plasma distribution are examined for different discharge conditions, and validated with available experiments from literature. Furthermore, a comparison is made between GAP and MW plasma. The GAP operates at atmospheric pressure, while the MW plasma experiments to which comparison is made were performed at reduced pressure. Indeed, the MW discharge region becomes very much contracted near atmospheric pressure, at the conditions under study, as revealed by our 2D model. The models predict that thermal reactions play the most important role in H_2S decomposition in both plasma types. The GAP has a higher energy efficiency but lower conversion than the MW plasma at their typical conditions. When compared at the same conversion, the GAP exhibits a higher energy efficiency and lower energy cost than the MW plasma.

Keywords: Hydrogen sulphide, plasma, gliding arc, microwave, conversion

1. Introduction

Hydrogen sulfide (H_2S) is produced in large amounts from hydrocarbon upgrading processes associated with petroleum refining and natural gas industries. H_2S is a byproduct of hydro-desulfurization and often comprises a significant portion of natural gas deposits. It is currently treated via the Claus process. A gross reaction of the Claus process is partial oxidation of H_2S to S_{solid} and H_2O [1]. This process, even though well established, has the major drawback of oxidizing valuable H_2, which could be used for hydro-desulfurization and, of course, for many other applications, including "green" energy generation. H_2S can be a good source for H_2 production, since its dissociation enthalpy to H_2 and S_{solid} is only 0.2 eV/molec. However, sulphur is normally not produced in the condensed phase, and the high temperature required for the H_2S decomposition yields sulfur in the form of the dimer S_2, which requires a higher enthalpy of 0.9 eV/molec. Nevertheless, this enthalpy is still quite low, compared to the dissociation enthalpy of liquid water, which is 2.96 eV/molec [2]. Unfortunately, an economically feasible process that could accomplish this dissociation has not yet been implemented at

large scale. Non-thermal plasma (NTP) is an attractive alternative energy source for unconventional reactions that typically demand severe operating conditions [3,4]. NTP decomposition of H_2S towards H_2 and sulphur may be quite promising for the effective utilization of H_2S. The major advantage of the direct decomposition of H_2S compared to the conventional Claus process is thus the production of H_2. H_2 is a valuable product used as raw material in the chemical industry and as feedstock in fuel cells for clean energy production [5].

Multiple works have been reported on the decomposition of H_2S by NTP [6–14]. Traus et al. investigated the H_2S decomposition in a dielectric barrier discharge (DBD) at atmospheric pressure, and pointed out a low decomposition rate (0.5–12%) and a high energy cost (50 eV/molec) [6]. The same authors found a better conversion in a rotating glow discharge (~ 40%), but the energy cost was still high (around 27 eV/molec) [7]. The energy costs were also reported very high (~ 100 eV/molec) in pulsed corona discharges, with low H_2S concentrations (~ 1%) [8,9]. Zhao et al. showed that the energy costs strongly depend on the gas composition: when using He or Ar, a much lower energy cost of ~17 eV/molec could be achieved than when using H_2 (~65 eV/molec) [10].

Gliding arc (GA) plasmas are among the most effective and promising plasmas for gas conversion [2,4,15], because they offer benefits of both thermal and non-thermal discharges. They are typically considered as 'warm' discharges: their power and temperature are high enough for intensive chemical conversion, while they are still non-equilibrium plasmas. In a PhD thesis from Drexel University, T. Nunnally [11] showed that a reverse vortex flow GA plasma, also called gliding arc plasmatron (GAP), is the most promising type for H_2S decomposition, in terms of conversion and energy efficiency. He obtained a maximum conversion around 40% and lowest energy cost of 7 eV/molec [11]. In addition, microwave (MW) plasmas might provide very high energy efficiency, due to a combination of relatively high electron density and low reduced electric field, which favour the gas dissociation [12–14]. The best values reported (conversion of 81% at energy cost of 2 eV/molec) were obtained in a MW plasma at reduced pressure (0.1 atm) [14]. Besides, MW plasma has another advantage of electrode-less set up, and hence there is no problem of limited electrode lifetime (no wearing out). In fact, this advantage also partially applies to the GAP: it has electrodes, but the vortex gas flow around the hot plasma arc isolates the latter from the walls, thus avoiding that the arc is in contact with the walls. Nevertheless, the arc is still attached at the electrodes, which may cause electrode degradation due to its high temperature.

Besides experiments, detailed modelling is very useful to provide more insight into the underlying reaction mechanisms of plasma-assisted gas conversion or synthesis, e.g. by evaluating quantities which are difficult to measure, and by identifying the most important chemical reactions or parameters. The kinetics of thermal non-catalytic H_2S decomposition has been studied [16–18], but to our knowledge, no papers exist yet on modelling both the detailed chemical kinetics and species transport in plasma-based H_2S decomposition. Therefore, in this paper, we investigate H_2S decomposition by means of computer modelling, for both a GAP and a MW plasma, to elucidate the underlying mechanisms in both

plasma types. More specifically, we use a combination of zero-dimensional (0D) chemical kinetics modeling, to describe the plasma chemistry at typical GAP and MW plasma conditions, and two-dimensional (2D) plasma fluid dynamics modeling, to describe the gas flow pattern and plasma characteristics in both types of plasma reactors. The simulation results are validated with experiments from literature [11,12] as much as possible, to make sure they yield reliable predictions. Note that we compare an atmospheric pressure GA and reduced pressure MW plasma, not so much to judge which one is better, but rather to evaluate the performance and to understand the underlying chemistry of two types of plasma reactors at different conditions, that have been used in practice.

2. Description of the models

2.1 Zero-dimensional (0D) chemical kinetics model

We use a 0D chemical kinetics model, called ZDPlaskin [19], to elucidate the plasma chemistry in both the GAP and MW plasma. In this model, the time-evolution of the species densities is calculated by balance equations, taking into account the various production and loss terms, as defined by the chemical reactions. This balance equation is solved for all plasma species, i.e., electrons, various types of molecules, radicals, ions and excited species (see below):

$$\frac{dn_i}{dt} = \sum_j \left\{ \left(a_{ij}^{(2)} - a_{ij}^{(1)} \right) k_j \prod_l n_l^{a_{lj}^{(1)}} \right\} \tag{1}$$

where $a_{ij}^{(1)}$ and $a_{ij}^{(2)}$ are the stoichiometric coefficients of species i, at the left and right hand side of a reaction j, respectively, n_l is the species density at the left-hand side of the reaction, and k_j is the rate coefficient of reaction j (see below).

The species considered in the model are listed in table 1. The model considers 34 different species, including the electrons, various molecules, radicals, ions and excited species.

Table 1: Overview of the species included in the model. H_2(V1-V15) denote the vibrational levels, while the other excited species are electronically excited levels. No vibrational levels of H_2S could be included, because of lack of data.

Molecules	Charged species	Radicals	Excited species
H_2, S_2, H_2S	H_2S^+, S^+, H^+, H^-, H_2^+, H_3^+, electrons	H, SH, S, H_2S_2	H_2(V1-V15), H_2(B3), H_2(B1), H_2(A3), H_2(A1), H(2P)

These species react with each other through 85 electron impact reactions, 11 ion-neutral and ion-ion reactions, and 303 neutral reactions. These reactions, along with their rate coefficients and the references where these data are adopted from, are listed in the Appendix. The rate coefficients of the heavy particle reactions (i.e., atoms, molecules, radicals, ions, excited species) depend on the gas

temperature, whereas the rate coefficients for the electron impact reactions are a function of the electron temperature and calculated from the electron energy distribution function (EEDF):

$$k_j = \int_0^\infty \sigma_j(\varepsilon) f_\varepsilon(\varepsilon) \sqrt{\frac{2\varepsilon}{m_e}} \, d\varepsilon \qquad (2)$$

ε is the electron energy, $\sigma_j(\varepsilon)$ the cross section of the jth reaction, $f_e(\varepsilon)$ the EEDF and m_e the mass of an electron (9.1094×10^{-31} kg).

The EEDF is calculated with a Boltzmann solver, BOLSIG[+] [20], which is integrated into ZDPlaskin, based on all electron impact cross sections, including also superelastic collisions. The electron impact cross sections of momentum transfer, attachment and ionization of H_2S are from [21], while the cross sections for H_2, H, S_2 and S are based on [22,23]. These cross sections are plotted as a function of electron energy in the Appendix.

Transport processes are neglected in this 0D model; hence, the species densities are assumed to be uniform in the entire simulation volume, and only evolve as a function of time. However, we can translate the temporal behavior (as calculated in the model) into a spatial behavior (i.e., as a function of distance along the reactor) by means of the experimental gas flow rate [24–26].

The calculations are run for a fixed residence time of the gas in the plasma reactor, as defined by the experimental gas flow rate and reactor (plasma) length (see Figure 1 below). In practice, the gas flow rate was 2 slm for the GAP, and it was varied between 0.4 and 1.6 slm in the MW experiments. Thus, the residence time in the model was 2.36 ms for the GAP, and between 0.1376 s and 0.5504 s for the MW plasma. The time-step used in this model is variable during the simulation (starting from 10^{-12} s and gradually increasing by a factor 1.01 in each time step, to save calculation time). The power deposition is used as input in the model, and it determines the electric field in the plasma. We varied the power from 120 W to 400 W for the GAP and from 300 W to 1000 W for the MW plasma.

This model does not only calculate the species densities, but also provides information about the H_2S decomposition and H_2 yield, and about the energy cost and energy efficiency, based on the H_2S conversion and specific energy input. The H_2S conversion into H_2 at the reactor outlet (exit) is defined as:

$$\chi_C(\%) = \frac{nH_2(e)v(e)}{nH_2S(0)v(0)} \times 100\% \qquad (3)$$

where nH_2 is the total H_2 density (calculated in this model) and v is the gas velocity as defined by mass conservation law (obtained with the 2D model below, based on the experimental gas flow velocity, mentioned above). The value in the denominator is the H_2S inlet flow density.

The energy efficiency (η) and energy cost (*EC*) as calculated by:

$$\eta \ (\%) = \frac{\chi_c \ (\%) \times \Delta H \ (\frac{eV}{molec})}{SEI \ (\frac{eV}{molec})} \tag{4}$$

$$EC \left(\frac{eV}{molec}\right) = \frac{SEI \left(\frac{eV}{molec}\right)}{\chi_c \ (\%)} \times 100\% \tag{5}$$

χ_c is the H_2S conversion, ΔH=0.9 eV/molec is the enthalpy for H_2S decomposition into H_2 and ½ S_2, and SEI is the specific energy input, which is calculated from the plasma power and the gas flow rate:

$$SEI \ (J/cm^3 \ ) \ = \ SEI \ (kJ/L) \ = = \frac{Pplasma \ (kW) \times 60 \ (s \ /min)}{gas \ flow \ rate \ (L/min \ )} \times 100\% \tag{6}$$

It can also be expressed in eV/molec, as used in eq. (5) above:

$$SEI \ (eV/molec \ ) \ = \frac{SEI \ (kJ/L) \times Vmol \ (L/ \ mol \ ) \times 10^3 \ (J/ \ kJ \ )}{1.6 \times 10^{-19}(J/eV) \times 6.02 \times 10^{23}(molec/ \ mol \ )} \times 100\% \tag{7}$$

Vmol is the molar volume, being equal to 24.5 L mol^{-1} (at room temperature and 1 atm). Note that the SEI is indeed calculated based on the molar volume at room temperature, as this is the condition at which the gas is inserted in the reactor.

2.2 2D fluid dynamics model

We developed the 2D fluid dynamics model within COMSOL Multiphysics software, which is a powerful interactive environment for modeling and solving all kinds of scientific and engineering problems, based on partial differential equations (PDEs). COMSOL Multiphysics internally compiles a set of equations representing the entire model.

2.2.1 Gas flow equations

For a proper description of the GAP and MW plasma, we need to describe the gas flow, which is responsible for the arc displacement (in the GAP) and for the plasma distribution (in the MW plasma). The gas flow rate in GAP and MW plasmas is in the order of 1 slm (or higher), so the gas velocities can be very high inside the reactors (see reactor dimensions in figure 1 below), suggesting a highly turbulent gas flow.

In fluid and gas flows, turbulence stands for rapid oscillations of velocity and pressure, varying over a wide range both in space and time. In contrast to laminar flows, which are quite predictive, turbulent flows are much more chaotic in nature, requiring a greater amount of computing power to be calculated numerically. The gas flow is simulated in our model using the so-called k-ε Reynolds-averaged Navier–Stokes (RANS) turbulent modelling technique, as shown in equations (8-9), which

effectively averages all fluctuating turbulent quantities over time, greatly reducing the computational cost [27,28].

$$\nabla \cdot (\rho \overrightarrow{u_g}) = 0 \tag{8}$$

$$\rho(\overrightarrow{u_g} \cdot \nabla)\overrightarrow{u_g} = \nabla \cdot [-p\vec{I} + (\mu + \mu_{Tu})\left(\nabla \overrightarrow{u_g} + \nabla \left(\overrightarrow{u_g}\right)^T\right) - \frac{2}{3}(\mu + \mu_{Tu})(\nabla \cdot \overrightarrow{u_g})\vec{I} - \frac{2}{3}\rho k_{Tu}\vec{I}] + \vec{F} \tag{9}$$

Here, ρ stands for the gas density, $\overrightarrow{u_g}$ is the gas flow velocity vector, superscript T stands for transposition, p is the gas pressure, μ is the dynamic viscosity of the fluid, μ_{Tu} is the turbulent viscosity of the fluid, k_{Tu} is the turbulent kinetic energy, $\vec{I}$ is the unity tensor and $\vec{F}$ is the body force vector. Equations (8) and (9) are coupled with two more transport equations, describing the turbulent kinetic energy and the turbulent dissipation rate. More details can be found in [27,28]. As for the boundary conditions, the inlets are defined as gas flow normal velocity boundaries, and the outlet is defined as a zero-gradient outflow boundary. All walls permit no flux and confirm the no-slip condition. Consequently, the RANS model is able to compute the flow field, which would usually contain small turbulent oscillations (eddies), as a time-averaged quantity. The final solution is the gas flow velocity throughout the entire GAP and MW reactor.

2.2.2 Turbulent Heat Transfer equation

Gas heating is usually an important phenomenon in GAP and MW plasmas as well. Here we calculate the gas temperature by solving the gas thermal balance:

$$\rho C_p \frac{\partial T_g}{\partial t} + \rho C_p \overrightarrow{u_g} \cdot \nabla T_g - \nabla \cdot ((k_g + k_T)\nabla T_g) = Q \tag{10}$$

where C_p is the specific heat capacity of the gas, k_g is the temperature-dependent gas thermal conductivity (based on a material look-up table), k_T is the turbulent heat conductivity of the fluid, T_g is the gas temperature, and Q accounts for the gas heating due to elastic and inelastic collisions between electrons and heavy particles in the plasma. More details can be found in ref [29].

2.2.3 Particle balance equations

The equations responsible for the plasma description (i.e. the particle balance for the electrons, the various ions, radicals, molecules and excited species, and the electron energy balance) are the same in the models for GAP and MW plasma. We use the drift–diffusion approximation and we solve the well-known particle balance equation:

$$\frac{\partial n_s}{\partial t} + \nabla \cdot G_s + (\overrightarrow{u_g} \cdot \nabla)n_s = R_e \tag{11}$$

Where n_s is the species density, G_s is the species flux, $\overrightarrow{u_g}$ is the gas velocity and R_e is the collision source term. The flux of the different species is expressed as follows:

$$G_s = -D_s\,\nabla(n_s) + \frac{q_s}{|q_s|}\mu_s n_s E \tag{12}$$

Where D_s is the diffusion coefficient and μ_s is the mobility of the corresponding species, E is the electric field vector and q_s is the charge of the given species type. For neutral species, the flux is only determined by diffusion.

2.2.4 Electron energy balance equation

The averaged electron energy is calculated by solving:

$$\frac{\partial n_e \varepsilon}{\partial t} + \nabla\cdot(-\mu_\varepsilon n_e E\text{-}D_\varepsilon\,\nabla(n_e\varepsilon)) + (\overrightarrow{u_g}\cdot\nabla)n_e\varepsilon{=}q_e E\cdot G_e + n_e\Delta\varepsilon + Q_{bg} \tag{13}$$

Where Q_{bg} stands for the stabilizing background heat source (background power density) and ε is the average electron energy. The terms μ_ε and D_ε stand for the energy mobility and diffusion, respectively:

$$\mu_\varepsilon = \frac{5}{3}\mu_e \tag{14}$$

$$D_\varepsilon = \frac{2}{3}\mu_\varepsilon\varepsilon \tag{15}$$

The electric field is either calculated from the well-known Poisson equation (for the MW plasma), or from the charge conservation equation (for the GAP).

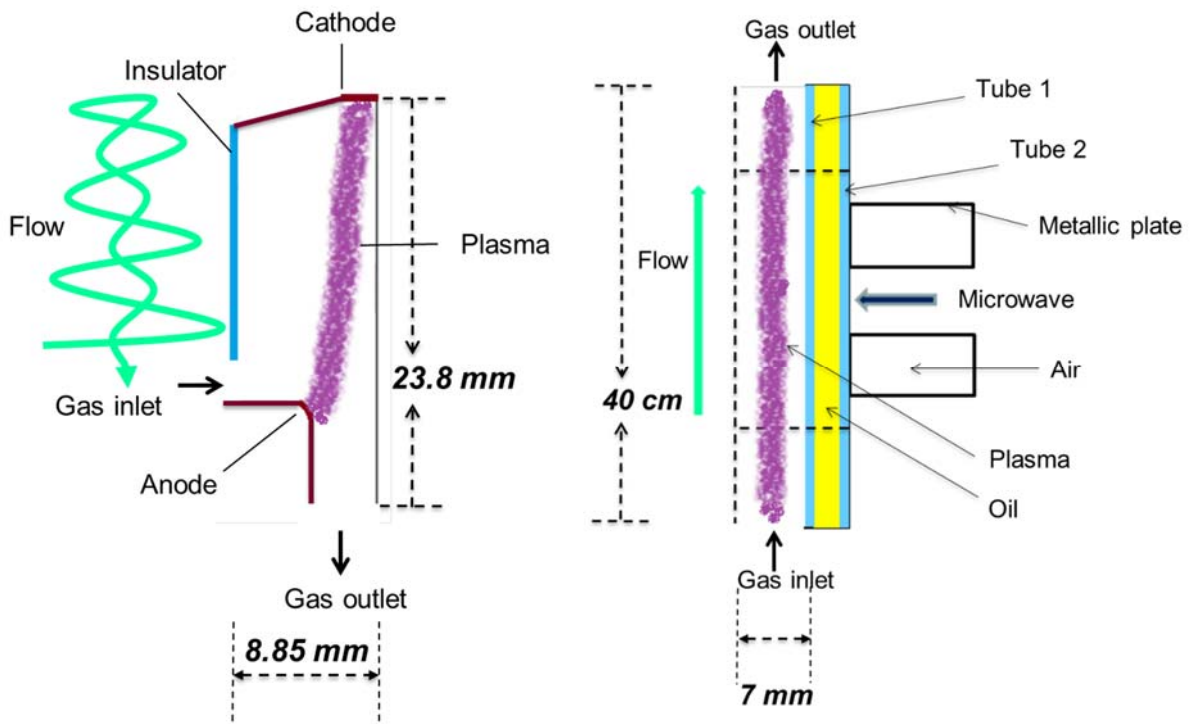### 2.2.5. Model geometry for the GAP and MW plasma

Figure 1: GAP geometry (left) [30] and MW geometry (right) [31] used in the 2D model. In both cases,

only one half plane of the cylindrically symmetrical reactors is shown, with the symmetry axis at the right for the GAP, and at the left for the MW plasma. The plasma is in both cases schematically indicated with purple color, while the gas flow is represented in green.

Figure 1 illustrates the geometries used in the COMSOL model for GAP and MW plasma. As both reactors are axisymmetric, we only simulate one half plane of the reactors, as seen in figure 1, to save calculation time. For the GAP, the voltage is applied to the anode, while the cathode is grounded, and the arc is formed between both electrodes, as schematically indicated in the figure. For the MW plasma, the microwaves propagate into the reactor, originating from the waveguide, and they develop along the reactor sidewall, inducing a plasma discharge inside Tube 1, as also schematically illustrated in the figure.

3. Results and discussion

3.1. Model validation

First we will validate the plasma chemistry included in the models by comparison with experiments, for both the GAP and MW plasma. This is necessary, so that we can trust the model predictions on the underlying mechanisms.

3.1.1. GAP: Calculated H_2S conversion, energy efficiency and energy cost

We applied the 0D model to the conditions typical for a GAP [11], i.e., atmospheric pressure, gas flow rate of 2 slm, and specific energy input (SEI) of 1.45 eV/molec (which corresponds to 5.7 kJ/L). In addition, to validate the model, we have also varied the SEI (from 0.8 to 3 eV/molec; or 3.15 – 11.8 kJ/L) and pressure (from 0.1 to 1 atm), keeping the other parameters constant, and we compared these calculation results with the experimental data as well. The gas temperature is an input in our 0D model, but it has not been measured in the arc. However, we estimate it in the order of 2000 – 3000 K, based on literature and our own calculations for a GAP in CO_2 [32]. At constant gas flow rate, a higher SEI means a rising discharge power and hence rising gas temperature. We assume a linear increase in gas temperature as a function of SEI (and hence discharge power), from 2300 K at atmospheric pressure, 2 slm and 0.8 eV/molec, to 2400 K at 1.45 eV/molec, and to 2600 K at 3 eV/molec, which is in the range of expectations.

Figure 2 shows the influence of SEI on the calculated H_2S conversion into H_2, energy efficiency, and energy cost, at atmospheric pressure and a gas flow rate of 2 slm. For comparison, the assumed gas temperature and calculated equilibrium conversion at these temperatures, as a function of SEI, are also plotted, for thermal (non-plasma) conditions. In the latter case, the SEI is also calculated by the ratio of power over gas flow rate, like for the plasma simulations, and we assume the same power as the plasma power, but we only consider thermal (neutral) reactions, at the temperature created by this power, hence no electron impact reactions.

The equilibrium conversion ranges between 91 and 95 % in this temperature (or SEI) range, hence much higher than the obtained conversion in the GAP. This indicates that the conversion inside the arc (which indeed operates at these high temperatures) is near 100 %, and proceeds by thermal reactions (as will be confirmed in section 3.2 below), but that the overall conversion obtained in the GAP is limited by the fraction of gas passing through the arc plasma.

The H_2S conversion increases almost linearly with rising SEI, whereas the energy efficiency first stays more or less constant, and then decreases. The energy cost shows the opposite trend as the energy efficiency, i.e. it increases with rising SEI. The reason is that the conversion first rises a bit faster with SEI, and then a bit more slowly, so the trends of the energy efficiency and energy cost follow directly from equations (4-5) above. However, the variation in energy efficiency and energy cost is fairly small. This means that overall, the higher SEI values will yield better results, because they give rise to significantly higher H_2S conversion into H_2, while the energy efficiency and energy cost are only slightly
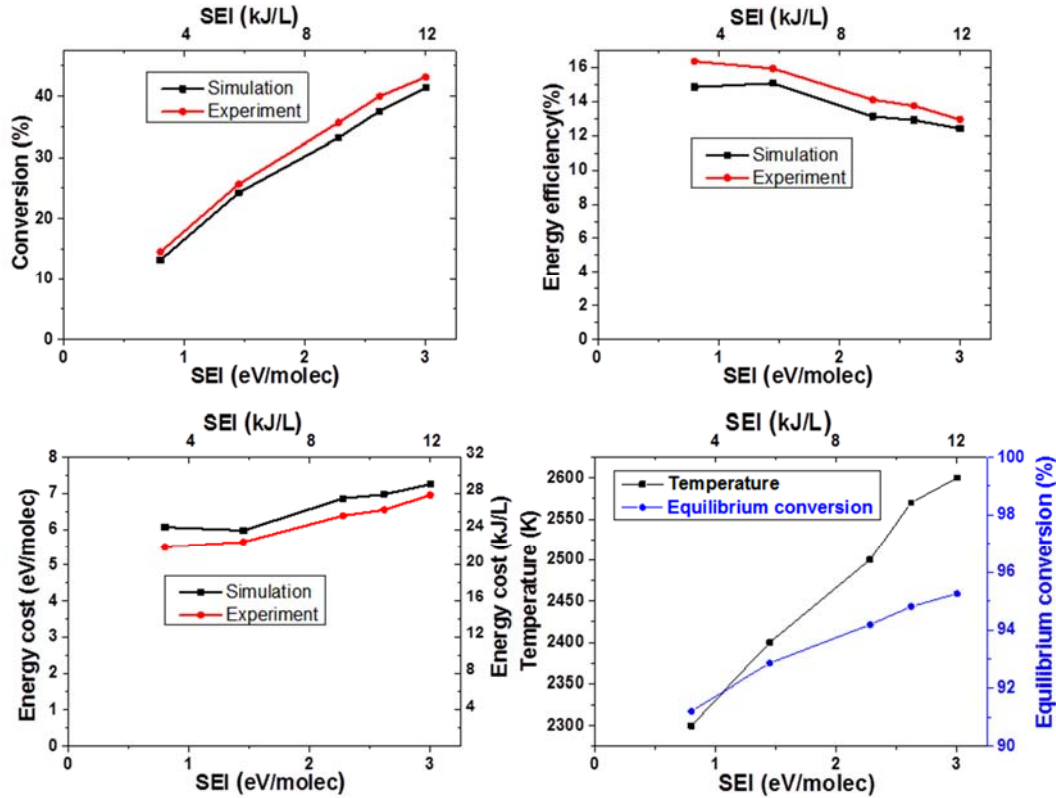
lower/higher, respectively.

Figure 2: Calculated H_2S conversion to H_2, energy efficiency, and energy cost, as a function of SEI (expressed both in eV/molec and in kJ/L), for a GAP at atmospheric pressure and a gas flow rate of 2 slm, and comparison with experimental results from literature [11]. The corresponding temperature (used as input in the model) and calculated equilibrium conversion as a function of SEI are also plotted.

The values obtained, i.e., H_2S conversion around 10 – 40 %, energy efficiency around 12 – 15 %, and energy cost around 6 – 7 eV/molec (which corresponds to 23.6 – 27.6 kJ/L) are in very good agreement with the experimental data obtained in the GAP [11], which validates our model assumptions and reaction set.

Although a GAP typically operates at atmospheric pressure, Nunally et al. investigated the effect of pressure [11], so we applied our model to the same conditions, again to validate the model. Figure 3 shows the influence of operating pressure on the H_2S conversion, energy efficiency, and energy cost, for an SEI of 1.45 eV/molec at a gas flow rate of 2 slm. The corresponding temperatures and equilibrium conversions are also plotted. As predicted by our 2D fluid dynamics simulations, a lower pressure yields a somewhat wider arc discharge volume. This is accounted for in our 0D model by assuming a somewhat larger fraction of gas passing through the arc, which leads to a larger overall conversion. For a fixed SEI, the higher conversion yields a higher energy efficiency and a lower energy cost. Again, very good agreement is reached with the experimental data [7].
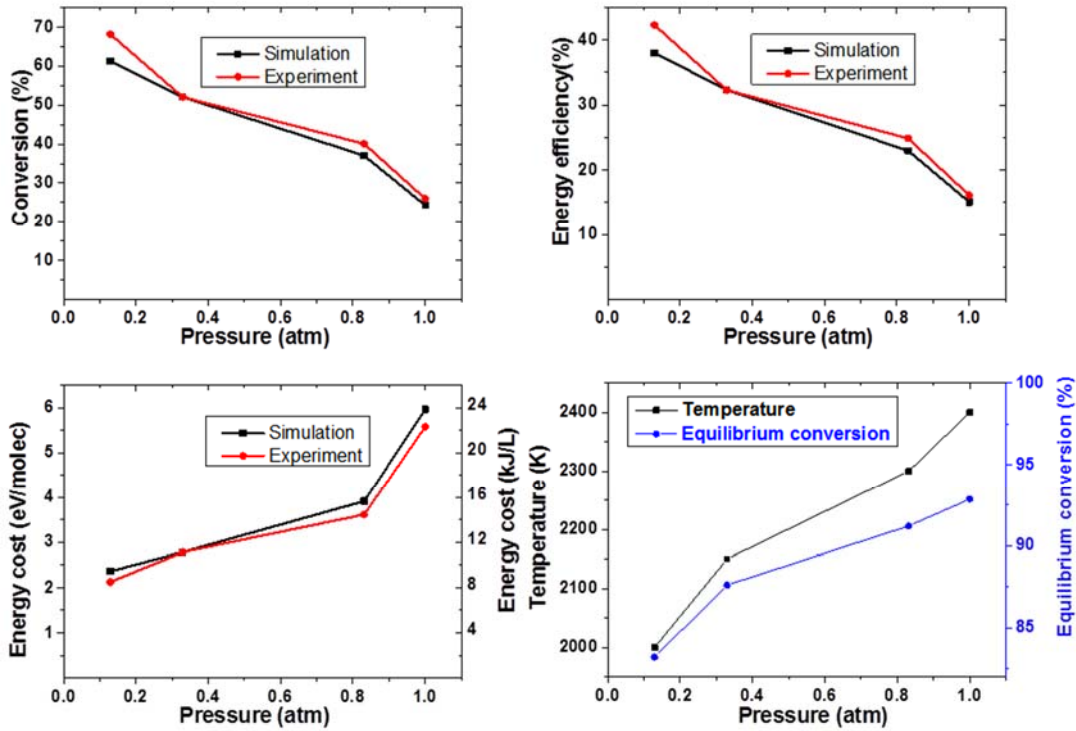
Figure 3: Calculated H_2S conversion to H_2, energy efficiency, energy cost, and corresponding temperature (used as input in the model) and calculated equilibrium conversion, as a function of pressure, for a GAP, at an SEI of 1.45 eV/molec (or 5.7 kJ/L), and a gas flow rate of 2 slm, and comparison with experimental results from literature [11].

3.1.2. MW plasma: Calculated H_2S conversion, energy efficiency and energy cost

To validate the model for the MW plasma, we compared with experimental data obtained from [12], at a pressure of 0.02 atm and a power of 1000 W. In a MW plasma, the gas temperature can also be fairly high. However, we had no data available for the experimental conditions under study, so we first calculated the gas temperature by our 2D model, and we incorporated these calculation results in our 0D model.

Figure A.2 in the Appendix displays the gas temperature distribution obtained with the 2D calculations, for the experimental data under study, i.e., 0.02 atm and 1000 W, and two different gas flow rates. The gas temperature only slightly increases with rising gas flow rate, from maximum values of 2830 K at 0.125 slm, to around 2900 K at 0.4 slm. In our 0D simulations, we need a spatially-averaged gas temperature, and based on Figure A.2, we estimate this to be around 2500 K, and we slightly adjust this value in the 0D simulations for different gas flow rates, as illustrated in Figure A.3 of the Appendix.

Figure 4 shows the influence of gas flow rate on the H_2S conversion into H_2, energy efficiency, and energy cost. Good agreement between simulations and experiments was achieved. Not only the conversion, energy efficiency and energy cost were compared, but also the SEI with varying gas flow rate. As the gas temperature is calculated at each time step, and slightly changes with time during the

simulation, which affect the gas flow rate a bit, the calculated SEIs are not exactly the same as the experimental values, but still very close. The gas residence time in the discharge volume decreases with rising gas flow rate, which reduces the conversion. As we fix the applied power to 1000 W, in line with the experimental conditions [12], the SEI thus significantly decreases with increasing gas flow rate (because SEI = power / gas flow rate), as illustrated in Figure 4. As a result, the energy efficiency significantly increases, and the energy cost drops upon rising gas flow rate. As the drop in conversion with increasing gas flow rate is more modest than the rise in energy efficiency (and drop in energy cost), it is clear that the higher gas flow rate yields overall the best results. Again, we also illustrate the temperature and equilibrium conversion as a function of gas flow rate. As the temperature in the MW plasma is also very high, comparable to the GAP, the equilibrium conversion is also in the order of 93 – 95 %. When comparing to the calculated conversion in the MW plasma in Figure 4, we can conclude that a larger fraction of the gas (H_2S) passes through the plasma than for the GAP, which is indeed like expected, because at this low pressure, the MW plasma will take up a quite large volume of the reactor, as predicted by our 2D fluid dynamics simulations (see section 3.3 below) and used as input in our 0D model to evaluate the fraction of gas passing through the plasma.
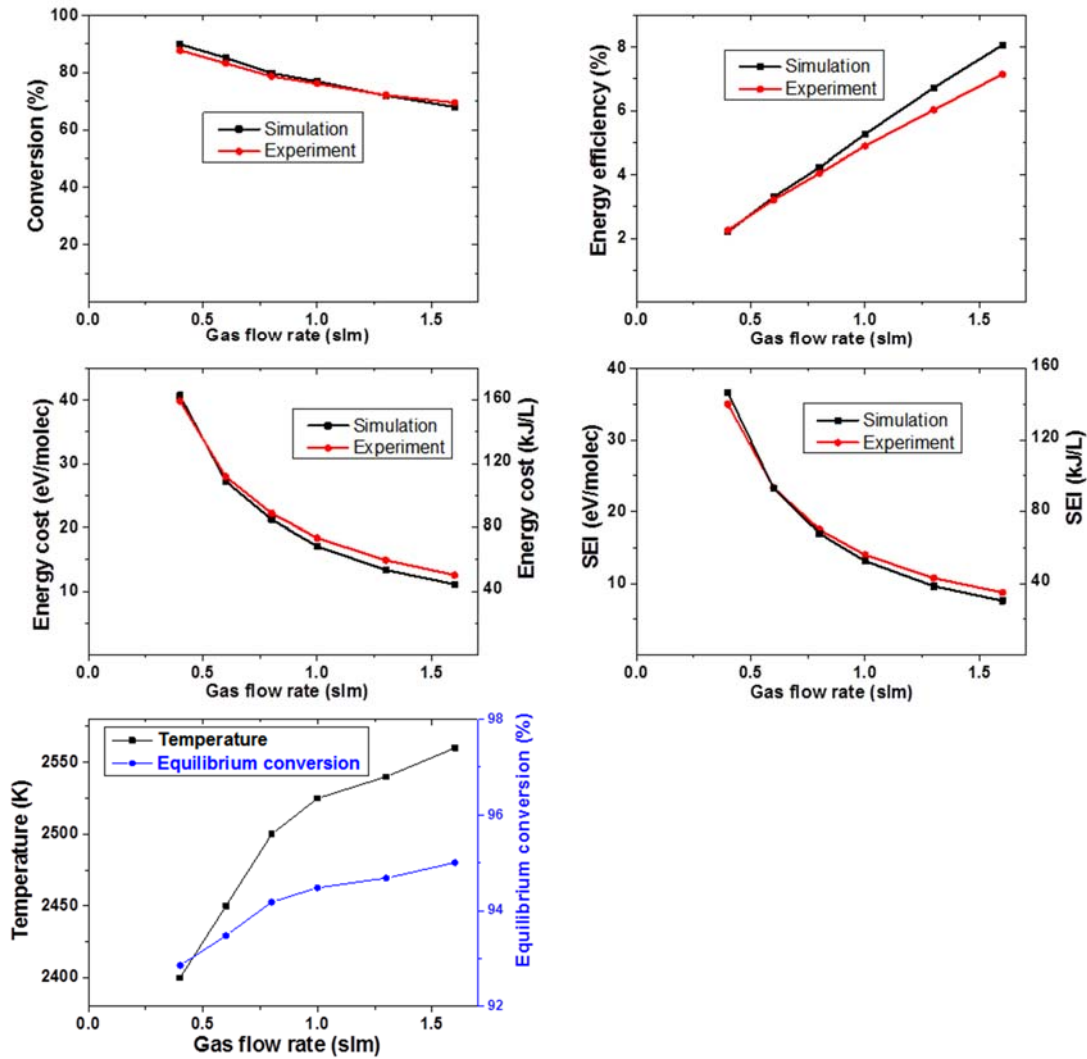
Figure 4: Calculated H_2S conversion to H_2, energy efficiency, energy cost, SEI, temperature and corresponding equilibrium conversion, as a function of gas flow rate, for a MW plasma, at a pressure of 0.02 atm and 1000 W, and comparison with experimental data from [12].

In Figure 5 we plot the H_2S conversion, energy efficiency, energy cost, as well as the corresponding temperatures and equilibrium conversions, as a function of SEI, for a gas flow rate of 1 slm, at 0.02 atm. Comparison is again made with experimental data from [12], and reasonable agreement is reached. Although the conversion significantly increases with rising SEI, the energy efficiency monotonously decreases, and the energy cost increases. The reason can easily be understood from equations (4-5) above, because the conversion rises not so fast as the SEI. It means that the increased power input is not only consumed for H_2S decomposition into H_2, but also for other reactions. Depending on what is most desired for the application, i.e., high conversion (with lower energy efficiency and higher energy cost), or high energy efficiency with low energy cost (but lower conversion), either a higher SEI or lower SEI might be more beneficial. At an intermediate SEI of 8 eV/molec (or 31.5 kJ/L), a quite high conversion of 65 %, in combination with a reasonable energy efficiency above 7 %, and energy cost around 12

eV/molec (or 47 kJ/L) is reached. It must be kept in mind, however, that these results are obtained at reduced pressure of 0.02 atm, which is less compatible with industrial applications, and the energy cost of pumping is not included here.
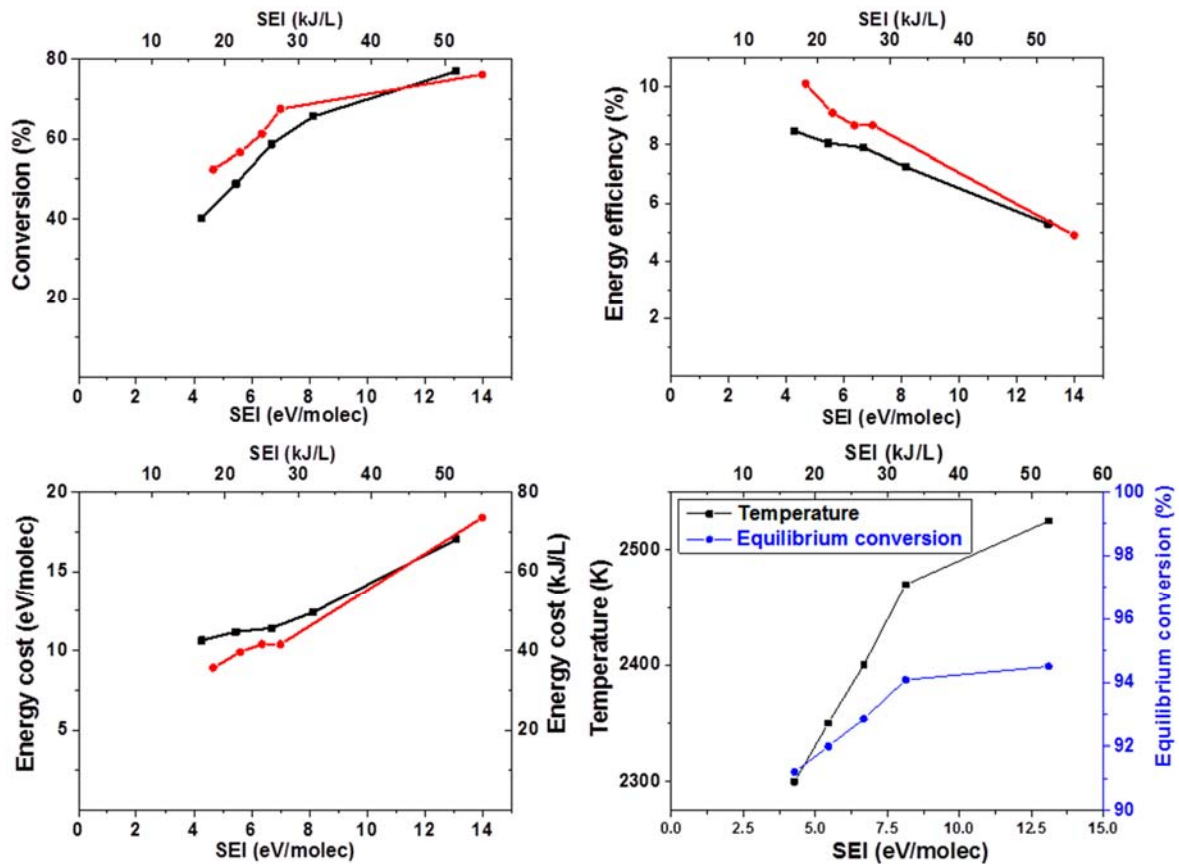

Figure 5: Calculated H$_2$S conversion to H$_2$, energy efficiency, energy cost, temperature and equilibrium conversion, as a function of SEI (expressed both in eV/molec and kJ/L), for a MW plasma, at a gas flow rate of 1 slm, and 0.02 atm, and comparison with the experimental results of [12].

3.2. Underlying chemistry: reaction pathways for H$_2$S decomposition in GAP and MW plasma

Figure 6 shows the species number densities as a function of time in both the GAP (a) and MW plasma (b), for their typical operating conditions, i.e., pressure of 1 atm, gas flow rate of 2 slm, and SEI of 1.45 eV/molec for the GAP, and pressure of 0.02 atm, gas flow rate of 1 slm, and SEI of 8.4 eV/molec for the MW plasma. The gas residence time in the GAP is 2.36 ms, while it is 0.344 s in the MW plasma.

Our model predicts a continuous dissociation of H$_2$S towards the production of H$_2$ and S$_2$ as a function of time, or distance travelled by the gas through the GAP and MW plasma. Other species such as SH and HS$_2$ also show significant number densities, almost comparable to those of H$_2$ and S$_2$, but they are intermediate species, so their densities stay constant and don't rise with time, as is clearly the case for the end products, i.e. H$_2$ and S$_2$. Specifically, as seen in figure 6(a) and (b), H$_2$S first dissociates

into SH, H, H_2 and H_2S_2, and subsequently SH and H_2S_2 react to produce HS_2. HS_2 further reacts with SH to form S_2 and again H_2S, which leads to a significant increase of the S_2 density. Furthermore, the abundant amount of S_2 recombines with H to generate again HS_2, which leads to a dramatic decrease of the H density. As the recombination reaction between S_2 and H is so fast, S_2 and H cannot have a high density at the same time, i.e. once the S_2 density increases, the H density will drop, and vice versa. Eventually, the H density keeps decreasing and the S_2 density keeps increasing with time and it becomes one of the main products.

The corresponding reaction mechanism is illustrated in figure 7. In general, large amounts of intermediate species, such as SH, H, HS_2 and H_2S_2 are produced during the decomposition of H_2S. These intermediate species will further react with each other and largely contribute to the regeneration of H_2S, during which also plenty amounts of H_2 and S_2 are produced and gradually become the end products. As the pressure in the MW discharge (figure 6(b)) is much lower than in the GA (figure 6(a)), the evolutions of species density is a bit more fluctuating with time.
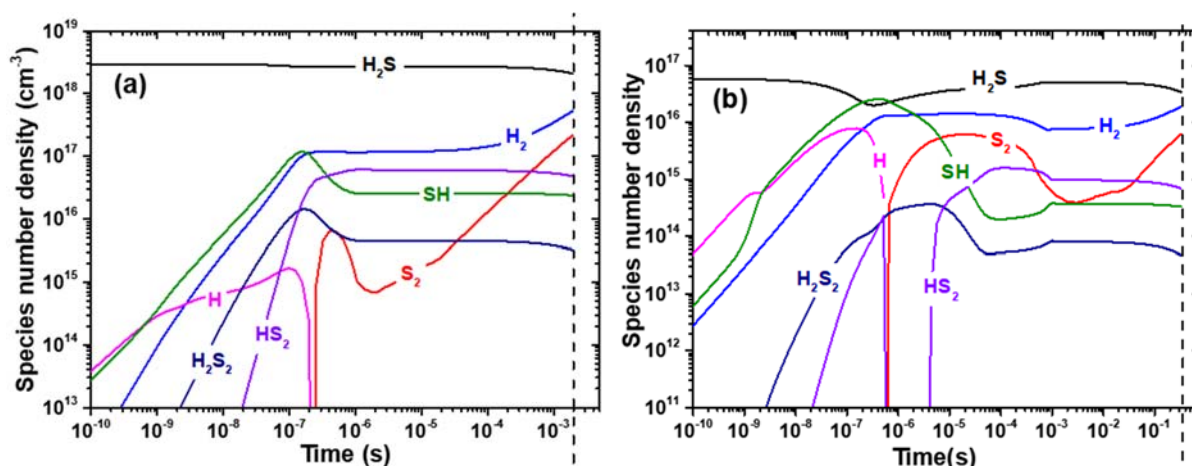

Fig. 6 Calculated number densities of various species as a function of time, for the GAP at a pressure of 1 atm, gas flow rate of 2 slm and SEI of 1.45 eV/molec (a), and for the MW plasma at a pressure of 0.02 atm, gas flow rate of 1 slm and SEI of 8.4 eV/molec (b). The residence time in the plasma in both cases is indicated with the vertical dashed line.

Our calculations predict that thermal dissociation via neutral species reactions contributes most to the dissociation of H_2S (confirming the conclusions drawn in section 3.1 above). Indeed, the most significant processes towards the splitting of H_2S are direct thermal dissociation ($H_2S + M \rightarrow H + SH + M$; where M denotes any species in the plasma) as well as the collision between H_2S and SH ($H_2S + SH \rightarrow H_2S_2 + H$), as indicated in Figure 7. They have a relative contribution of 48% and 51%, respectively, to the H_2S splitting in the GAP, and 58% and 41%, respectively, in the MW plasma. In contrast, the relative contribution from direct electron impact processes is lower than 1%.

The H radicals produced from H_2S splitting can give rise to H_2 formation, but the major part of H are consumed for the generation of HS_2, which further reacts with SH, leading to the regeneration of H_2S (see figure 7). Hence, the net contribution of the above dissociation processes is much lower, and

the most important H_2S decomposition process overall, leading to the formation of H_2, is direct thermal dissociation of H_2S ($H_2S + M \rightarrow H_2 + S + M$) (see Figure 7), with a relative contribution of 75% and 76% in the GAP and MW plasma, respectively. Other important reactions leading to the production of H_2 include the collision of H_2S with H ($H_2S + H \rightarrow SH + H_2$) as well as the collision between two SH species ($SH + SH \rightarrow S_2 + H_2$). They have relative contributions of 23% and 2%, respectively, in the GAP, and 23% and 1% in the MW plasma. In general, large intermediate concentrations of SH and H are generated during the decomposition of H_2S, as was also clear from Figure 6, which play an important role in the formation of H_2, but they also greatly contribute to the regeneration of H_2S.

S_2 is also a significant product of H_2S conversion (see Figure 6). The most important production process of S_2 is the reaction of SH with HS_2, producing H_2S and S_2, with a relative contribution of 93%. The reaction of HS_2 with S atoms ($S + HS_2 \rightarrow SH + S_2$) also contributes to S_2 formation, with a relative contributions of 6 % in both the GAP and MW plasma.
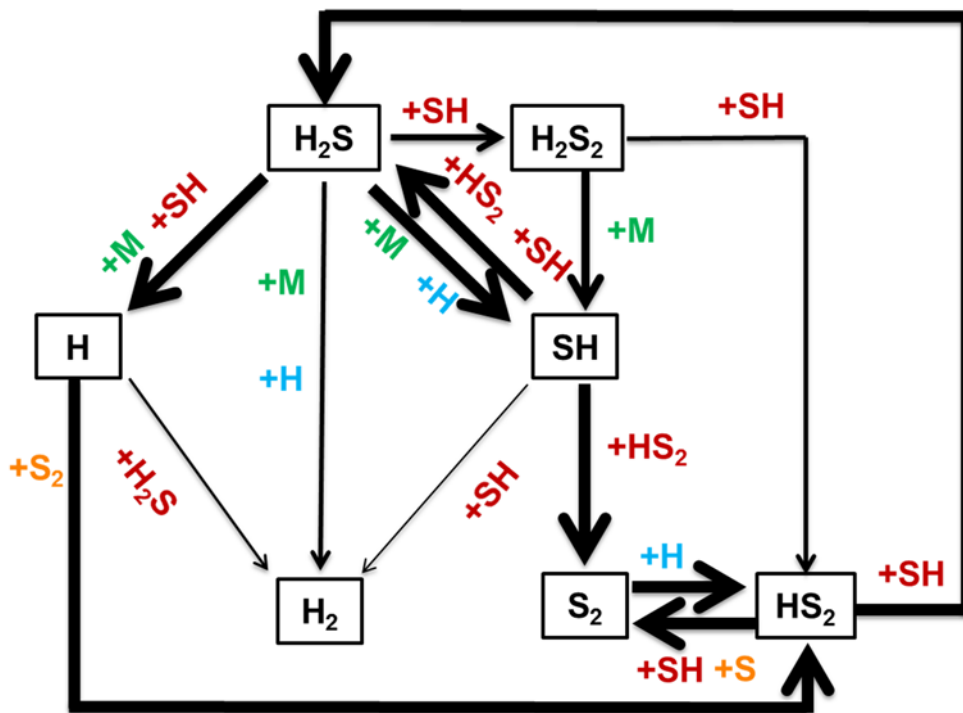

Figure 7: Reaction scheme of the main pathways of H_2S decomposition in the GAP and MW plasma, as predicted by our model. The thickness of the arrow lines corresponds to the importance of the reactions. They appear to be very similar for both the GAP and MW plasma (see text). M denotes any plasma species.

3.3. Comparison of GAP and MW plasma: 2D simulation results

Figure 8 shows the calculated distribution of electron density, gas temperature, and H_2 density in the GAP, at atmospheric pressure, an applied power of 1000 W and gas flow rate of 2 slm, corresponding to an SEI of 0.8 eV/molec. The arc is formed between the cathode (top) and anode (bottom). The highest gas temperature (around 2760 K) is reached near both electrodes,

where the strongest electric field can be found, but it is quite high in the entire arc channel, giving rise to strong H_2S decomposition in the entire arc region, generating a broad H_2 density distribution, with high density (almost 3×10^{20} m^{-3}).
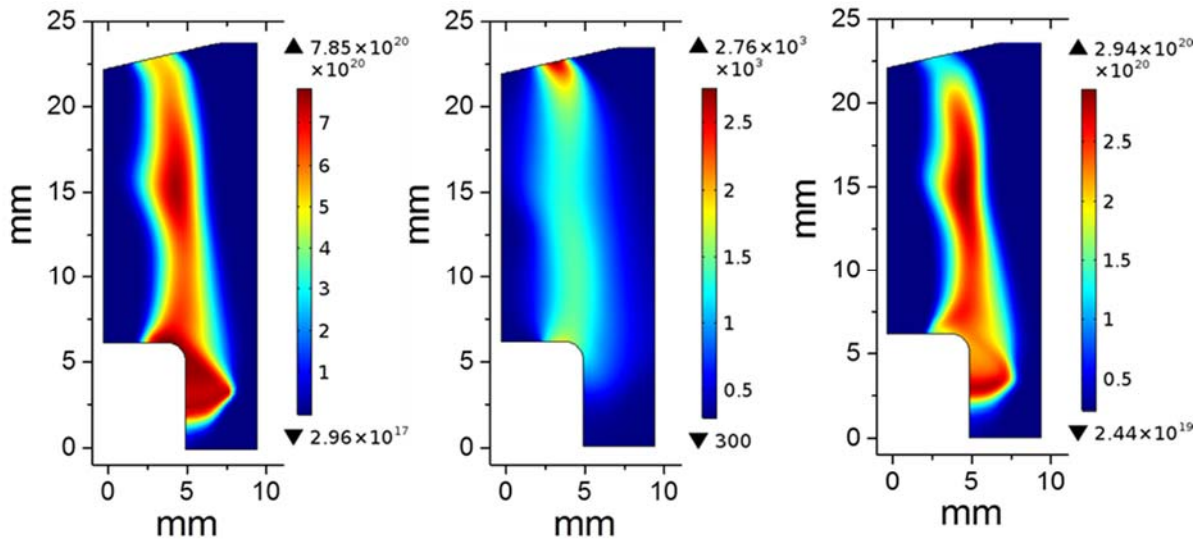

Figure 8: Calculated electron density (left, in m^{-3}), gas temperature (middle, in K), and H_2 density (right, in m^{-3}) in the GAP, obtained from the 2D simulations, at atmospheric pressure, with 1000 W applied power and 2 slm gas flow rate, corresponding to an SEI of 0.8 eV/molec.

Figure 9 shows the distribution of electron density, gas temperature, and H_2 density in the MW plasma, at 0.02 atm, an applied power of 1000 W and a gas flow rate of 0.4 slm, yielding an SEI of 14 eV/molec. The plasma is generated in a large area, with a gas temperature of almost 3000 K. Many local maxima appear along the tube, which induce a relatively uniform plasma distribution. This results in a high H_2S decomposition, yielding a H_2 density of 1.2×10^{22} m^{-3}.
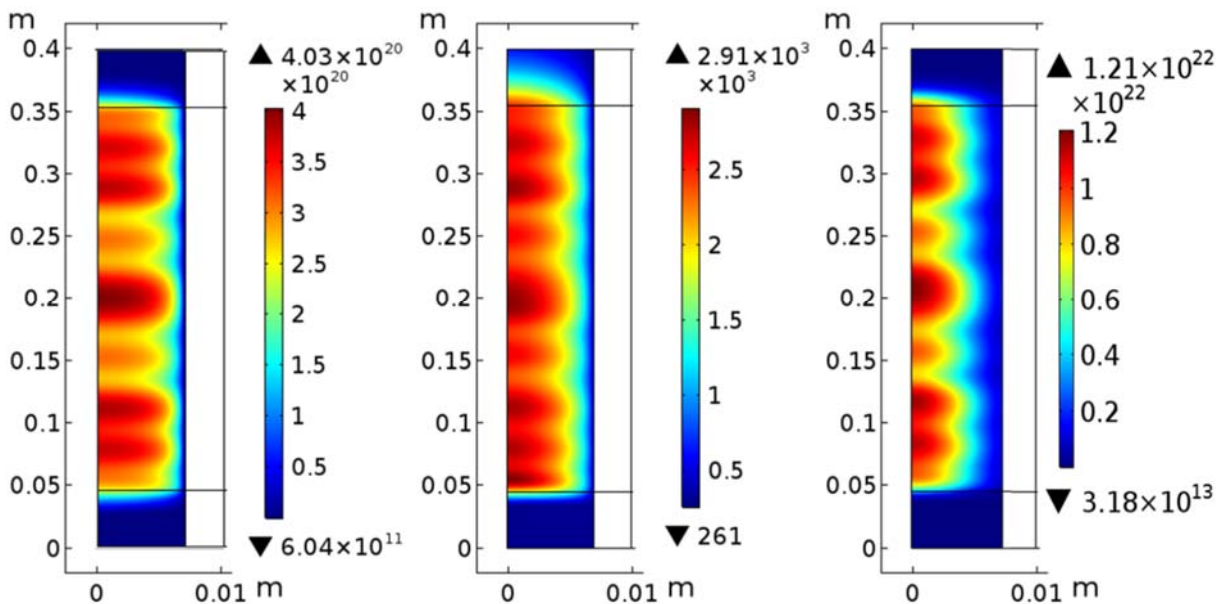
Figure 9: Calculated electron density (left; in m^{-3}), gas temperature (middle; in K), and H_2 density (right; in m^{-3}) in the MW plasma, obtained from the 2D simulations, at 0.02 atm with 1000 W applied power and 0.4 slm gas flow rate, corresponding to an SEI of 14 eV/molec.

We were not able to run the 2D model for the MW plasma at atmospheric pressure, which would be more beneficial for industrial applications, due to stability problems at 1000 W power. However, to examine the influence of pressure on the H_2S decomposition in the MW discharge, we plot in Figure 10 the H_2 density distribution, obtained from the 2D simulations, at 0.02 and 0.5 atm, for a lower power of 100 W. In both cases, the plasma is much more confined to the center, instead of filling the entire reactor. Note that the H_2 density is two orders of magnitude higher at 0.5 atm than at 0.02 atm, i.e., reaching values of 5×10^{23} m^{-3}, but the right figure is plotted in the same scale as the left figure, for easy comparison. In spite of the much higher H_2 density, this density is confined only to a very small region, much smaller than at 0.02 atm. Moreover, it originates from a higher H_2S density, due to the higher pressure (which is a factor 25 higher). Hence, the overall H_2S conversion, obtained from the H_2 density integrated over the entire reactor volume, is estimated to be only 0.0048 % at 0.5 atm, while it is 0.127 % at 0.02 atm. Note that this very low conversion is due to the very low applied power of 100 W. Besides, to obtain accurate values of the conversion, it must be calculated from the flux at the outlet, and not by integrating the density over the reactor volume. Thus, the 0D model gives a better representation of the conversion rate, but at least the 2D model gives an indication of the effect of pressure.
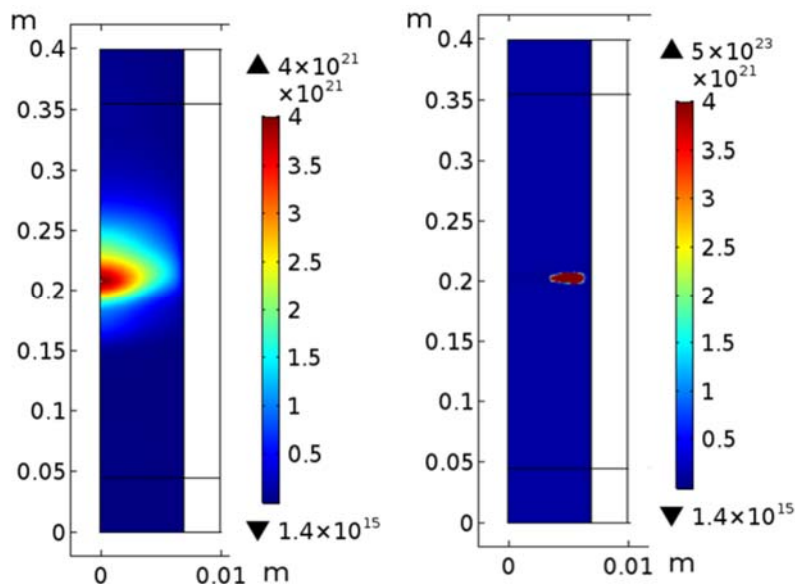

Figure 10: Calculated H_2 density distribution (in m^{-3}) in a MW plasma, obtained from the 2D simulations, at 0.02 atm (left) and 0.5 atm (right), at 100 W applied power. Note that the maximum H_2 density at 0.5 atm is around 5×10^{23} m^{-3}, but the figure is plotted in the same color scale as the left figure, for easy comparison.

Figure 10 illustrates that the MW plasma is indeed very contracted at the higher pressure of 0.5 atm, yielding a much smaller discharge volume than at 0.02 atm (around 10 times difference), which explains the much lower conversion. The difference is even more pronounced at higher power input. Indeed, as shown in Figure 9 above, at 1000 W, the discharge volume at the low pressure of 0.02 atm was much broader, while at higher pressure, our calculations reveal that it remains very contracted. In addition, this extremely contracted discharge was also causing unstable simulations, as the power density becomes extremely high in the contracted volume. Therefore, we were not able to perform 2D simulations at pressures close to atmospheric pressure. This corresponds to the experiments, where only data at low pressure of 0.02 atm were reported [12], probably because the MW plasma could not be operated (or gave a very low conversion) at higher pressure. We expect that a vortex gas flow – as also applied to the GAP – could stabilize the MW plasma at atmospheric pressure as well, as demonstrated for CO_2 conversion [33]. However, for the basic MW plasma under study here, atmospheric pressure operation seemed not feasible. Therefore, we can only compare here the performance of the GAP (typically operating at atmospheric pressure) with the MW plasma at reduced pressure.

3.4. Comparison of GAP and MW plasma: Performance in terms of H_2S conversion, energy efficiency and energy cost

In Figure 11 we plot the energy efficiency and energy cost vs conversion, in both the GAP and MW plasma, at their typical discharge conditions, adopted from the experiments in ref [11], and ref [12], respectively, and indicated in the figure caption. The conversion is generally lower in the GAP (12 - 42 %) than in the MW plasma (38 - 78 %), whereas the energy efficiency is much higher (12.5 - 15% in the GAP, vs 5 – 8.5 % in the MW plasma), and consequently, the energy cost in the GAP (6 – 7.3 eV/molec, or 24 – 28.5 kJ/L) is also much smaller than in the MW plasma (10.6 - 17 eV/molec, or 41.75 - 70 kJ/L). When comparing at the same conversion of 40 %, the energy efficiency in the GAP is 12.5 %, while it is 8.5 % in the MW plasma, and the corresponding energy cost in the GAP is 7 eV/molec (or 27.6 kJ/L), whereas it is 11 eV/molec (or 43.3 kJ/L) in the MW plasma. This would indicate that the GAP is more suitable for H_2S decomposition, except when a very high conversion is targeted, which seems not feasible in the GAP at the typical experimental conditions investigated (see figure caption).
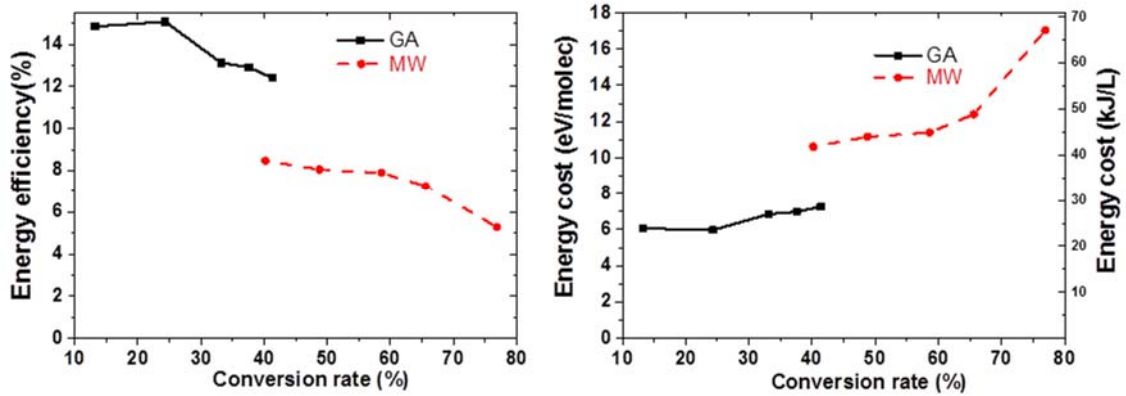
Figure 11: Energy efficiency and energy cost vs conversion, in GAP and MW plasma, at their typical conditions, i.e., 1 atm pressure, 2 slm gas flow rate, SEI from 0.8 eV/molec to 3 eV/molec for the GAP, and 0.02 atm pressure, 1 slm gas flow rate, SEI from 4.2 eV/molec to 13.1 eV/molec for the MW plasma.

In addition, it should be mentioned that the GAP results are obtained at atmospheric pressure, which is more compatible with industrial application than the low pressure of 0.02 atm in the MW plasma. When comparing figures 8 and 10, we can see that the plasma still has a quite broad discharge volume in the GAP, even at atmospheric pressure, which is more beneficial for gas conversion than the MW plasma under study here, which is very much contracted at (or close to) atmospheric pressure. This indicates that the GAP discharge may be a better option at high pressure, although vortex flow stabilization (similar to the one applied to the GAP), or other stabilization methods, could be applied to the MW plasma as well, but this would need further investigation.

Table 2. H_2 yield and energy cost, obtained in this work for both MW and GA plasma, and comparison with results reported in literature [6–10,13,14]. The energy cost is expressed in kWh/m³, to allow the comparison with literature. The results of ref [11,12] are not included here, as they are very similar to our computational results.

Plasma type	H_2 yield	Energy cost (kWh/m³)	Ref.
MW plasma in this work (0.02 atm)	40%	12	
	max 78%	19.4	
GA in this work (1 atm)	max 40%	7.7	
DBD (1 atm)	max 12%	55	[6]
Pulsed corona discharge (1.7 atm)	max 75%	206	[8]
Pulsed RF discharge	max 15%	110	[9]

(0.001 atm)			
Pulsed corona discharge (1 atm)	max 28%	18.7	[10]
Glow discharge (1 atm)	max 40%	30	[7]
MW plasma (0.95 atm)	max 32%	3.83	[13]
MW plasma (0.5 atm)	max 50.9%	4.13	[13]
MW plasma (0.1 atm)	45%	0.84	[14]
	max 81%	2.17	

Finally, we present in Table 2 our best results for both MW and GA plasma, in terms of H_2 yield and energy cost (in kWh/m^3), in comparison with data found in literature, to put our results in a broader perspective. The H_2 yield is generally better than in DBD or pulsed discharge, and quite comparable to glow discharge and MW plasmas from literature. It is clear that higher values can be reached in the MW plasma than in the GA, as also shown in Figure 11, but at a lower pressure. The energy cost of our MW and GA plasma is lower than for DBD, pulsed discharge and glow discharge from literature, but the MW plasmas in [13,14] reached a much lower energy cost than in our case. It should be noted, however, that the aim of our paper was not to optimize the H_2S conversion process, but rather to understand the underlying mechanisms in two promising types of plasma reactors. By careful optimization of the reactor design and operating conditions, as probably applied in [13,14], we should be able to reach better values, but this was outside the scope of the present paper. Nevertheless, the data from literature show that plasma can be quite promising for H_2S conversion, reaching fairly high H_2 yields and low energy costs.

4. Conclusion

We have investigated H_2S decomposition into H_2 and S_2 in a GAP and MW plasma, by means of 0D chemical kinetics modeling and 2D plasma fluid dynamics simulations, validated as much as possible by experiments from literature in a wide range of conditions. Our models predict that thermal dissociation via neutral species reactions (involving SH, H and HS_2) is most important for H_2S decomposition in both plasma sources.

Upon rising power, the gas temperature increases in both GAP and MW plasma, inducing a significantly higher H_2S conversion. However, the energy efficiency decreases (and the energy cost increases), as intermediate reactions also consume plenty of energy. A higher gas flow rate will reduce the gas residence time in both the GAP and MW plasma, which reduces the H_2S decomposition. Upon higher pressure, the plasma becomes more confined, as predicted from 2D simulations, which limits the fraction of gas passing through the plasma, and thus restricts the H_2S conversion. This is most striking in the MW plasma, where the discharge region becomes very much contracted, while the arc still has a

quite broad discharge volume in the GAP. This renders the GAP a better option at high pressure.

Generally, when comparing the GAP and MW plasma at their typical operating conditions studied here (i.e., GAP at atmospheric pressure and MW plasma at reduced pressure), the GAP exhibits a higher energy efficiency and lower energy cost, but a lower H_2S conversion. At high pressure (close to atmospheric pressure), which is most convenient for industrial operation, the MW plasma under study here becomes very contracted, leading to negligible H_2S conversion, which indicates that the GAP may be more suitable for H_2S decomposition, except when a very high conversion is targeted at low pressure. Nevertheless, it must be possible to apply stabilization methods to an atmospheric pressure MW plasma as well, as data from literature [13,14] illustrate H_2S decomposition in (near) atmospheric pressure MW plasma reactors at low energy cost. These MW plasma reactors were outside the scope of our study. Indeed, our study was intended to elucidate the underlying mechanisms of H_2S decomposition in GAP and MW plasma, but not to optimize the conditions. Nevertheless, the data from literature show that atmospheric pressure MW plasma can also be very suitable for H_2S decomposition.

Acknowledgments

Appendix

Table A.1: Electron impact reactions included in the model, as well as their rate coefficients and the references where these data are adopted from. For most electron impact reactions, the rate coefficients are calculated from the cross sections (indicated in the table as σ), which are plotted in Figure A.1 below.

Reaction	Cross section $\sigma(E)$/rate coefficient[a]	Reference
H_2S		
$e + H_2S \rightarrow e + SH + H$	$\sigma(E)$	[21]
$e + H_2S \rightarrow e + SH + H$	$\sigma(E)$	[21]
$e + H_2S \rightarrow e + S + H_2$	$\sigma(E)$	[21]
$e + H_2S \rightarrow e + S + 2H$	$\sigma(E)$	[21]
$e + H_2S \rightarrow e + e + H_2S^+$	$\sigma(E)$	[21]
$e + H_2S \rightarrow e + e + SH + H^+$	$\sigma(E)$	[21]

H₂

e + H₂ → e + H₂(e)[b]	σ(E)	[23]
e + H₂ → e + H₂(e)	σ(E)	[23]
e + H₂ → e + H₂(e)	σ(E)	[23]
e + H₂ → e + H₂(e)	σ(E)	[23]
e + H₂ → e + H₂(e)	σ(E)	[23]
e + H₂ → e + H₂(e)	σ(E)	[23]
e + H₂ → e + H₂(e)	σ(E)	[23]
e + H₂ → e + H₂(e)	σ(E)	[23]
e + H₂ → e + H₂(V1)[c]	σ(E)	[23]
e + H₂ → e + H₂(V1)	σ(E)	[23]
e + H₂ → e + H₂(V1)	σ(E)	[23]
e + H₂ → e + H + H	σ(E)	[23]
e + H₂ → e + e + H₂⁺	σ(E)	[23]
e + H₂(e) → e + H₂	σ(E)	[23]
e + H₂(e) → e + e + H₂⁺	σ(E)	[23]

H

e + H → e + H(2P)[b]	σ(E)	[23]
e + H → e + H(2P)	σ(E)	[23]
e + H → e + e + H⁺	σ(E)	[23]
e + H(2P) → e + H	σ(E)	[23]
e + H(2P) → e + H(2P)	σ(E)	[23]
e + H(2P) → e + e + H⁺	σ(E)	[23]
e + H⁻ → e + e + H	σ(E)	[23]
e + S → e + e + S⁺	σ(E)	[22]

Electron – ion recombination

Reaction	Rate coefficient	Reference
$e + e + H^+ \rightarrow H + e$	7.92×10^{-29}	[23]
$e + H_2^+ \rightarrow H + H$	$5.33\times10^{-8}\times(300.0/T_g)^{0.4}$	[23]
$e + H_2^+ \rightarrow H^+ + H^-$	$\sigma(E)$	[23]
$e + e + H_2^+ \rightarrow H_2 + e$	$8.80\times10^{-27}\times(300.0/T_g)^{4.5}$	[23]
$e + SH^+ \rightarrow S + H$	3.56×10^{-9}	[21]
$e + e + SH^+ \rightarrow SH + e$	7.92×10^{-29}	[21]
$e + H_2S^+ \rightarrow S + H_2$	3.70×10^{-09}	[21]
$e + H_2S^+ \rightarrow S + H + H$	2.89×10^{-08}	[21]
$e + H_2S^+ \rightarrow SH + H$	8.14×10^{-09}	[21]
$e + e + H_2S^+ \rightarrow H_2S + e$	7.92×10^{-29}	[21]

[a] The unit of the rate coefficient is cm^3s^{-1}, and T_g indicates the gas temperature (K), which can be several 1000 K at the conditions under study. Note that for most reactions we used temperature-dependent rate coefficients, but for some reactions, the temperature-dependence was not available, so we used constant rate coefficients.
[b] $H_2(e)$ and $H(2P)$ denote electronically excited species.
[c] $H_2(V1)$ denotes vibrationally excited species.

Table A.2: Ion-neutral and ion-ion reactions included in the model, as well as their rate coefficients and the references where these data are adopted from.

Reaction	Rate coefficient ($cm^3\ s^{-1}$)	Reference
$H^- + H \rightarrow H_2 + e$	1.30×10^{-9}	[23]
$H^- + H_3^+ \rightarrow H_2 + H + H$	1.0×10^{-7}	[23]
$H^- + H_2^+ \rightarrow H + H_2$	$2.0\times10^{-7}\times(T_g/300)^{-0.5}$	[23]
$H^- + H_2^+ \rightarrow H + H + H$	1.0×10^{-7}	[23]
$H^- + H_2^+ + M \rightarrow H + H_2 + M$	$2.0\times10^{-25}\times(T_g/300)^{-2.5}$	[23]
$H^+ + H^- \rightarrow H + H$	$2.0\times10^{-7}\times(T_g/300)^{-0.5}$	[23]
$H^+ + H^- + M \rightarrow H + H + M$	$2.0\times10^{-25}\times(T_g/300)^{-2.5}$	[23]
$H^- + H_2S^+ \rightarrow H_2S + H$	0.193×10^{-6}	[34]
$H^- + H_2S^+ \rightarrow H + H + SH$	0.1×10^{-6}	[34]
$H^+ + H_2 + M \rightarrow H_3^+ + M$	1.50×10^{-29}	[34]
$H^+ + H + M \rightarrow H_2^+ + M$	1.00×10^{-34}	[34]

Table A.3: Neutral reactions included in the model, as well as their rate coefficients and the references where these data are adopted from.

Reaction	Rate coefficient (cm^3 s^{-1})	Reference
$H + H + M \rightarrow H_2 + M$	$6.04 \times 10^{-33} \times (T_g/298)^{-1.0}$	[23]
$H + S + M \rightarrow SH + M$	$0.37 \times 10^{-33} \times (T_g/298)^{-0.6}$	[34]
$H_2(V1) + H_2 \rightarrow H_2 + H_2$	1.0×10^{-13}	[23]
$H_2(e) + H_2 \rightarrow H_2 + H_2$	1.0×10^{-13}	[23]
$H(2P) + H_2 \rightarrow H + H_2$	1.0×10^{-13}	[23]
$H_2S + M \rightarrow SH + H + M$	$2.92 \times 10^{-8} \times \exp(-33342.3/T_g)$	[35]
$H_2S \rightarrow S + H_2$	$3.16 \times 10^{-10} \times \exp(-32979.72/T_g)$	[36]
$H_2S + H \rightarrow SH + H_2$	$3.66 \times 10^{-12} \times (T_g/298)^{1.94} \times \exp(-453.23/T_g)$	[37]
$SH + S \rightarrow H + S_2$	4.0×10^{-11}	[38]
$SH + H \rightarrow S + H_2$	3.01×10^{-11}	[38]
$SH + SH \rightarrow S_2 + H_2$	1.0×10^{-14}	[38]
$SH + SH \rightarrow S + H_2S$	1.5×10^{-11}	[38]
$S_2 + M \rightarrow S + S + M$	$7.95 \times 10^{-11} \times \exp(-38755.83/T_g)$	[39]
$H_2 \rightarrow H + H$	$3.7 \times 10^{-11} \times \exp(-48384.38/T_g)$	[23]
$SH + H_2S \rightarrow H_2S_2 + H$	$3.32 \times 10^{-10} \times (T_g/298)^{0.5} \times \exp(-13596.77/T_g)$	[40]
$H_2S_2 + M \rightarrow SH + SH + M$	$3.43 \times 10^{-7} \times (T_g/298) \times \exp(-28764.72/T_g)$	[34]
$HS_2 + HS_2 \rightarrow H_2S_2 + S_2$	$3.46 \times 10^{-15} \times (T_g/298)^{3.37} \times \exp(840.99/T_g)$	[34]
$SH + HS_2 \rightarrow H_2S + S_2$	$3.66 \times 10^{-13} \times (T_g/298)^{3.05} \times \exp(553.94/T_g)$	[34]
$H + HS_2 \rightarrow H_2S + S$	$7.32 \times 10^{-11} \times \exp(-3182.65/T_g)$	[34]
$H + HS_2 \rightarrow H_2 + S_2$	$2.51 \times 10^{-11} \times (T_g/298)^{1.65} \times \exp(553.94/T_g)$	[34]
$S + HS_2 \rightarrow SH + S_2$	$2.0 \times 10^{-2} \times (T_g/298)^{2.20} \times \exp(302.15/T_g)$	[34]
$H_2S + M \rightarrow S + H_2 + M$	$2.66 \times (T_g)^{-2.61} \times \exp(-44904.59/T_g)$	[34]
$H_2S + S \rightarrow 2SH$	$1.38 \times 10^{-10} \times \exp(-3718.46/T_g)$	[41]
$S + H_2 \rightarrow SH + H$	$4.49 \times 10^{-11} \times \exp(-9714.14/T_g)$	[41]
$H + S_2 + M \rightarrow HS_2 + M$	$19.1 \times (T_g)^{-2.84} \times \exp(-838.47/T_g)$	[41]
$H + HS_2 \rightarrow 2SH$	4.98×10^{-10}	[34]
$H_2S_2 + H \rightarrow HS_2 + H_2$	$8.29 \times 10^{-17} \times (T_g)^{1.93} \times \exp(709.05/T_g)$	[34]

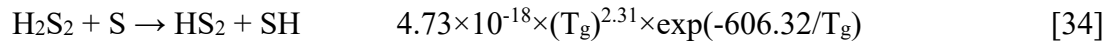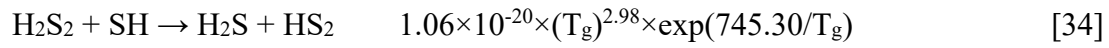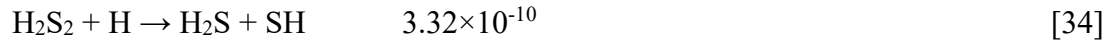|		
$H_2S_2 + H \rightarrow H_2S + SH$	3.32×10^{-10}	[34]
$H_2S_2 + SH \rightarrow H_2S + HS_2$	$1.06 \times 10^{-20} \times (T_g)^{2.98} \times \exp(745.30/T_g)$	[34]
$H_2S_2 + S \rightarrow HS_2 + SH$	$4.73 \times 10^{-18} \times (T_g)^{2.31} \times \exp(-606.32/T_g)$	[34]
$S_2 + M \rightarrow S + S + M$	$7.95 \times 10^{-11} \times \exp(-38775.97/T_g)$	[34]
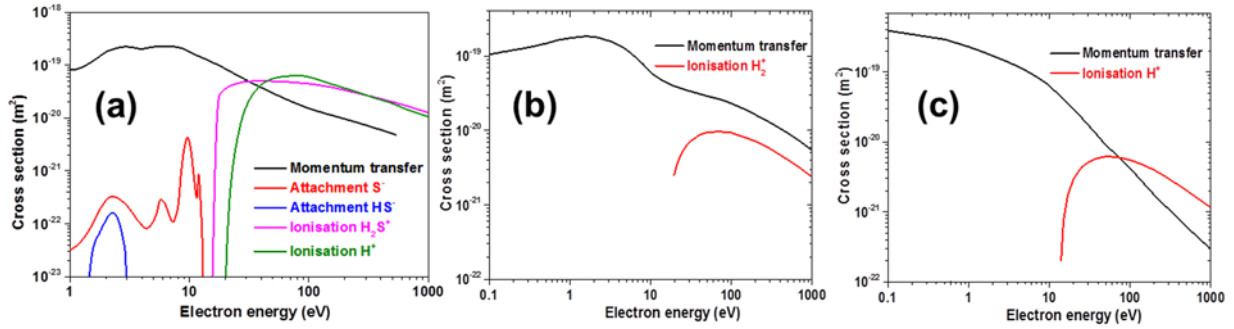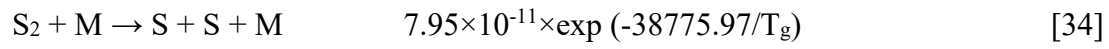
Figure A.1: Electron impact cross sections of momentum transfer, attachment and ionization of H_2S (a), momentum transfer and ionization of H_2 (b) and H (c) as a function of electron energy. These cross are adopted from[21,23].
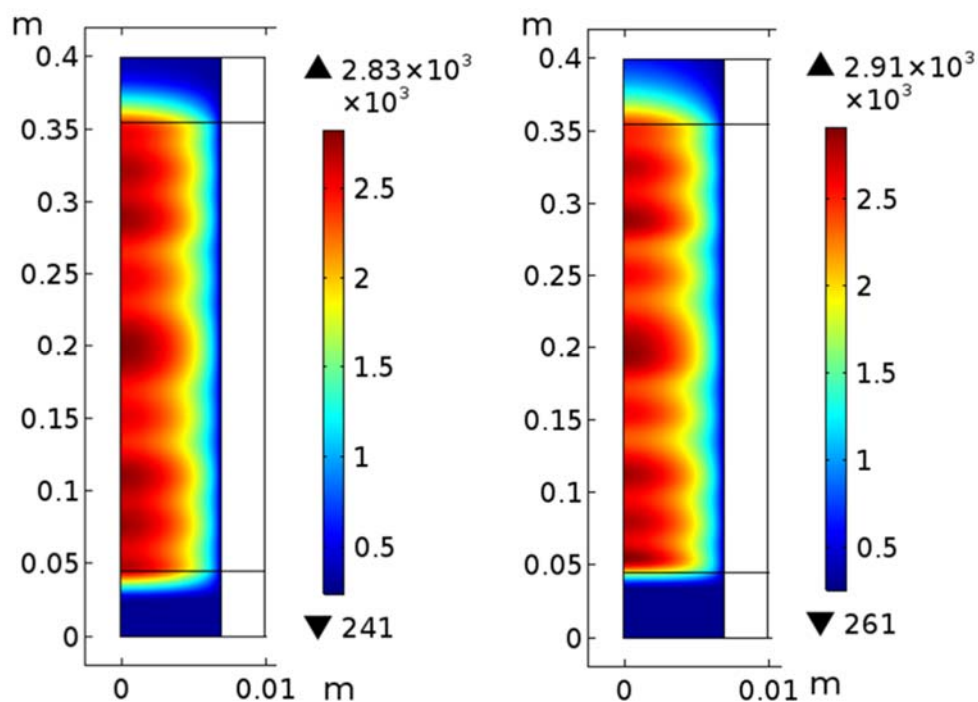
Figure A.2: Calculated gas temperature distribution in a MW plasma, obtained from our 2D calculations, for a gas flow rate of 0.125 slm (left) and 0.4 slm (right), at 0.02 atm and 1000 W, with SEI of 105 eV/molec and 35 eV/molec, respectively.
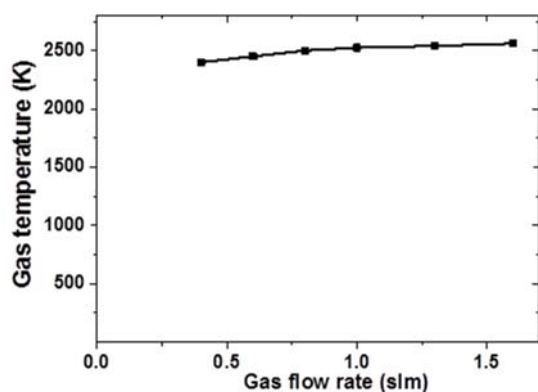

Figure A.3: Gas temperature used in the 0D model for the MW plasma, as a function of gas flow rate, based on the 2D simulations of Figure A.2.

References

[1]   Eow J S 2002 Recovery of sulfur from sour acid gas: A review of the technology *Environ. Prog.* **21** 143–62

[2]   Fridman A 2008 *Plasma chemistry* (Cambridge University Press)

[3]   Kim H-H 2004 Nonthermal Plasma Processing for Air-Pollution Control: A Historical Review, Current Issues, and Future Prospects *Plasma Process. Polym.* **1** 91–110

[4]   Snoeckx R and Bogaerts A 2017 Plasma technology – a novel solution for CO2 conversion? *Chem. Soc. Rev.* **46** 5805–63

[5]   Farrell A, Keith D W, Jensen M W and Ross M 2001 Hydrogen as a Transportation Fuel *Environ. Sci. Policy Sustain. Dev.* **43** 43–5

[6]   Traus I and Suhr H 1992 Hydrogen sulfide dissociation in ozonizer discharges and operation of ozonizers at elevated temperatures *Plasma Chem. Plasma Process.* **12** 275–85

[7]   Traus I, Suhr H, Harry J E and Evans D R 1993 Application of a rotating high-pressure glow discharge for the dissociation of hydrogen sulfide *Plasma Chem. Plasma Process.* **13** 77–91

[8]   Helfritch D J 1993 Pulsed corona discharge for hydrogen sulfide decomposition *IEEE Transactions on Industry Applications* vol 29 pp 882–6

[9]   Nicholas J E, Amodio C A and Baker M J 1979 Kinetics and mechanism of the decomposition of H2S, CH 3SH and (CH3)2S in a radio-frequency pulse discharge *J. Chem. Soc. Faraday Trans. 1 Phys. Chem. Condens. Phases* **75** 1868–75

[10]   Zhao G B, John S, Zhang J J, Hamann J C, Muknahallipatna S S, Legowski S, Ackerman J F and Argyle M D 2007 Production of hydrogen and sulfur from hydrogen sulfide in a nonthermal-plasma pulsed corona discharge reactor *Chem. Eng. Sci.* **62** 2216–27

[11]   Nunnally T P 2011 *Application of Low Current Gliding Arc Plasma Discharges for Hydrogen Sulfide Decomposition and Carbon Dioxide Emission Reduction, PhD Dissertation, Drexel University* (Drexel University)

[12]   Godefroid T 2016 *Traitement de mélange H2S par plasma micro-onde. Bilan de matière et énergétique* (Mons)

[13]   Luinstra E A, Energy A A and Research S 1995 *Hydrogen from H2S: Technologies and Economics* (Sulfotech Research)

[14]   Balebanov A V, Butylin B A, Zhivotov V K K V and Matolich R M M S 1985 Dissociation of hydrogen sulfide in a plasma *Dokludy Phys Chem* **283** 709

[15]   Gutsol A, Rabinovich A and Fridman A 2011 Combustion-assisted plasma in fuel conversion *J. Phys. D. Appl. Phys.* **44** 274001

[16]   Sassi M and Amira N 2012 Chemical reactor network modeling of a microwave plasma thermal decomposition of H2S into hydrogen and sulfur *Int. J. Hydrogen Energy* **37** 10010–9

[17]   Kaloidas V and Papayannakos N 1989 Kinetics of thermal, non-catalytic decomposition of hydrogen sulphide *Chem. Eng. Sci.* **44** 2493–500

[18]   Dowling N I and Clark P D 1999 Kinetic Modeling of the Reaction between Hydrogen and Sulfur and Opposing H2S Decomposition at High Temperatures *Ind. Eng. Chem. Res.* **38** 1369–75

[19]   Pancheshnyi S, Eismann B, Hagelaar G J M and Pitchford L C 2008 Computer code ZDPlasKin *Univ. Toulouse, LAPLACE, CNRS-UPS-INP, Toulouse, Fr.*

[20]   Hagelaar G J M and Pitchford L C 2005 Solving the Boltzmann equation to obtain electron transport coefficients and rate coefficients for fluid models *Plasma Sources Sci. Technol.* **14** 722

[21]   Rawat P, Iga I, Lee M-T, Brescansin L M, Homem M G P and Machado L E 2003 Cross sections for elastic electron--hydrogen sulfide collisions in the low-and intermediate-energy range *Phys. Rev. A* **68** 52711

[22]   Wang W, Murphy A B, Rong M, Looe H M and Spencer J W 2013 Investigation on critical breakdown electric field of hot sulfur hexafluoride/carbon tetrafluoride mixtures for high voltage circuit breaker applications *J. Appl. Phys.* **114** 103301

[23]   Wang W, Snoeckx R, Zhang X, Cha M S and Bogaerts A 2018 Modeling Plasma-based CO2 and CH4 Conversion in Mixtures with N2, O2, and H2O: The Bigger Plasma Chemistry Picture *J. Phys. Chem. C* **122** 8704–23

[24]   Aerts R, Somers W and Bogaerts A 2015 Carbon Dioxide Splitting in a Dielectric Barrier Discharge Plasma: A Combined Experimental and Computational Study *ChemSusChem* **8** 702–

16

[25]   Snoeckx R, Aerts R, Tu X and Bogaerts A 2013 Plasma-Based Dry Reforming: A Computational Study Ranging from the Nanoseconds to Seconds Time Scale *J. Phys. Chem. C* **117** 4957–70

[26]   Bogaerts A, Wang W, Berthelot A and Guerra V 2016 Modeling plasma-based {CO}2conversion: crucial role of the dissociation cross section *Plasma Sources Sci. Technol.* **25** 55016

[27]   Ferziger J H and Peric M 2012 *Computational methods for fluid dynamics* (Springer Science & Business Media)

[28]   Wilcox D C and others 1998 *Turbulence modeling for CFD* vol 2 (DCW industries La Canada, CA)

[29]   Kolev S and Bogaerts A 2015 A 2D model for a gliding arc discharge *Plasma Sources Sci. Technol.* **24** 15025

[30]   Ramakers M, Trenchev G, Heijkers S, Wang W and Bogaerts A 2017 Gliding Arc Plasmatron: Providing an Alternative Method for Carbon Dioxide Conversion. *ChemSusChem* **10** 2642–52

[31]   Georgieva V, Berthelot A, Silva T, Kolev S, Graef W, Britun N, Chen G, van der Mullen J, Godfroid T, Mihailova D and others 2017 Understanding Microwave Surface-Wave Sustained Plasmas at Intermediate Pressure by 2D Modeling and Experiments *Plasma Process. Polym.* **14** 1600185

[32]   Trenchev G, Kolev S, Wang W, Ramakers M and Bogaerts A 2017 CO2 Conversion in a Gliding Arc Plasmatron: Multidimensional Modeling for Improved Efficiency *J. Phys. Chem. C* **121** 24470–9

[33]   Bongers W, Bouwmeester H, Wolf B, Peeters F, Welzel S, van den Bekerom D, den Harder N, Goede A, Graswinckel M, Groen P W, Kopecki J, Leins M, van Rooij G, Schulz A, Walker M and van de Sanden R 2017 Plasma-driven dissociation of CO2 for fuel synthesis *Plasma Process. Polym.* **14** 1600126

[34]   Sendt K, Jazbec M and Haynes B S 2002 Chemical kinetic modeling of the H/S system: H2S thermolysis and H2 sulfidation *Proc. Combust. Inst.* **29** 2439–46

[35]   Tesner P A, Nemirovskii M S and Motyl D N 1991 Kinetics of the thermal decomposition of hydrogen sulfide at 600-1200 C *Kinet. Catal.* **31** 1081–3

[36]   Woiki D and Roth P 1994 Kinetics of the High-Temperature H2S Decomposition *J. Phys. Chem.* **98** 12958–63

[37]   Peng J, Hu X and Marshall P 1999 Experimental and ab Initio Investigations of the Kinetics of the Reaction of H Atoms with H2S *J. Phys. Chem. A* **103** 5307–11

[38]   Schofield K 1973 Evaluated Chemical Kinetic Rate Constants for Various Gas Phase Reactions *J. Phys. Chem. Ref. Data* **2** 25–84

[39]   Higashihara T, Saito K and Murakami I 1980 The Dissociation Rate of S2 Produced from COS Pyrolysis *Bull. Chem. Soc. Jpn.* **53** 15–8

[40]   Tiee J J, Wampler F B, Oldenborg R C and Rice W W 1981 Spectroscopy and reaction kinetics of HS radicals *Chem. Phys. Lett.* **82** 80–4

[41]   Shiina H, Oya M, Yamashita K, Miyoshi A and Matsui H 1996 Kinetic Studies on the Pyrolysis of H2S *J. Phys. Chem.* **100** 2136–40